

Bright Quantum Dot Single-Photon Emitters at Telecom Bands Heterogeneously Integrated on Si

P. Holewa^{1,2,*}, A. Sakanas², U. M. Gür³, P. Mrowiński¹, A. Huck⁴, B. Wang^{5,2}, A. Musiał¹, K. Yvind^{2,6}, N. Gregersen², M. Sypererek^{1,+}, and E. Semenova^{2,6,++}

¹Laboratory for Optical Spectroscopy of Nanostructures, Faculty of Fundamental Problems of Technology, Department of Experimental Physics, Wrocław University of Science and Technology, Wyb. Wyspiańskiego 27, 50-370 Wrocław, Poland

²DTU Fotonik, Technical University of Denmark, Kongens Lyngby 2800, Denmark

³DTU Electrical Engineering, Technical University of Denmark, 2800 Kongens Lyngby, Denmark

⁴Center for Macroscopic Quantum States (bigQ), Department of Physics, Technical University of Denmark, 2800 Kongens Lyngby, Denmark

⁵Hefei National Laboratory for Physical Sciences at Microscale, University of Science and Technology of China, Hefei, Anhui 230026, China

⁶NanoPhoton-Center for Nanophotonics, Technical University of Denmark, 2800 Kongens Lyngby, Denmark

*pawel.holewa@pwr.edu.pl

+marcin.sypererek@pwr.edu.pl

++esem@fotonik.dtu.dk

ABSTRACT

Whereas the Si photonic platform is highly attractive for scalable optical quantum information processing, it lacks practical solutions for efficient photon generation. Self-assembled semiconductor quantum dots (QDs) efficiently emitting photons in the telecom bands (1460-1625 nm) allow for heterogeneous integration with Si. In this work, we report on a novel, robust, and industry-compatible approach for achieving single-photon emission from InAs/InP QDs heterogeneously integrated with a Si substrate. As a proof of concept, we demonstrate a simple vertical emitting device, employing a metallic mirror beneath the QD emitter, and experimentally obtained photon extraction efficiencies of $\sim 10\%$. Nevertheless, the figures of merit of our structures are comparable with values previously only achieved for QDs emitting at shorter wavelength or by applying technically demanding fabrication processes. Our architecture and the simple fabrication procedure allows for the demonstration of a single-photon generation with purity $\mathcal{P} > 98\%$ at the liquid helium temperature and $\mathcal{P} = 75\%$ at 80 K.

Background

Exploiting single photons as a resource is a powerful approach for quantum information processing (QIP)¹⁻⁴. Photons have long coherences and efficiently propagate over macroscopic distances, which enabled the demonstration of a computational advantage with a quantum photonic processor⁵, loophole-free tests of Bell's theorem^{6,7}, and long distance quantum key distribution^{8,9}. Scalability of optical QIP requires the miniaturization, coupling and integration of active and passive photonic components into quantum photonic integrated circuits (QPICs)¹⁰. The Si-based photonic platform is a leading candidate for integration with transparency wavelengths $> 1.1 \mu\text{m}$ and mature manufacturing processes^{4,11}. QPICs supporting multi-dimensional entanglement¹¹ and quantum processors with hundreds of elements^{11,12} have been demonstrated. Si however does not allow for efficient light generation. Spontaneous four-wave mixing is the commonly employed approach for single photon generation on Si and realized with Si-on-insulator integration¹¹⁻¹³. This process is probabilistic with few-percent efficiency¹⁰, thus limiting scalability. Hybrid approaches combining solid-state single photon emitters (SPEs) with Si have instead been investigated¹⁴, but so far requiring technically demanding fabrication. The reliable realization of SPEs monolithically integrated with Si and allowing for the deterministic emission of pure single photons remains challenging.

Among different candidates^{15,16}, epitaxially grown self-assembled semiconductor quantum dots (QDs)¹⁷ emitting in the long-wavelength telecom bands (1460-1625 nm)¹⁸ are suitable for integration with Si^{11,19,20}. The telecom wavelength promises very low Si-waveguide propagation losses¹⁹ and allows for interconnecting distant QPICs using optical fiber networks and for distributed quantum computing^{21,22}. Photon emission in the telecom bands has been achieved with QDs based on either InAs/GaAs²³⁻²⁷ or InAs/InP²⁸⁻³⁶ material composition, and excellent quantum light sources with high purity and indistinguishability^{18,37} were demonstrated, fulfilling the requirements for QIP¹⁷.

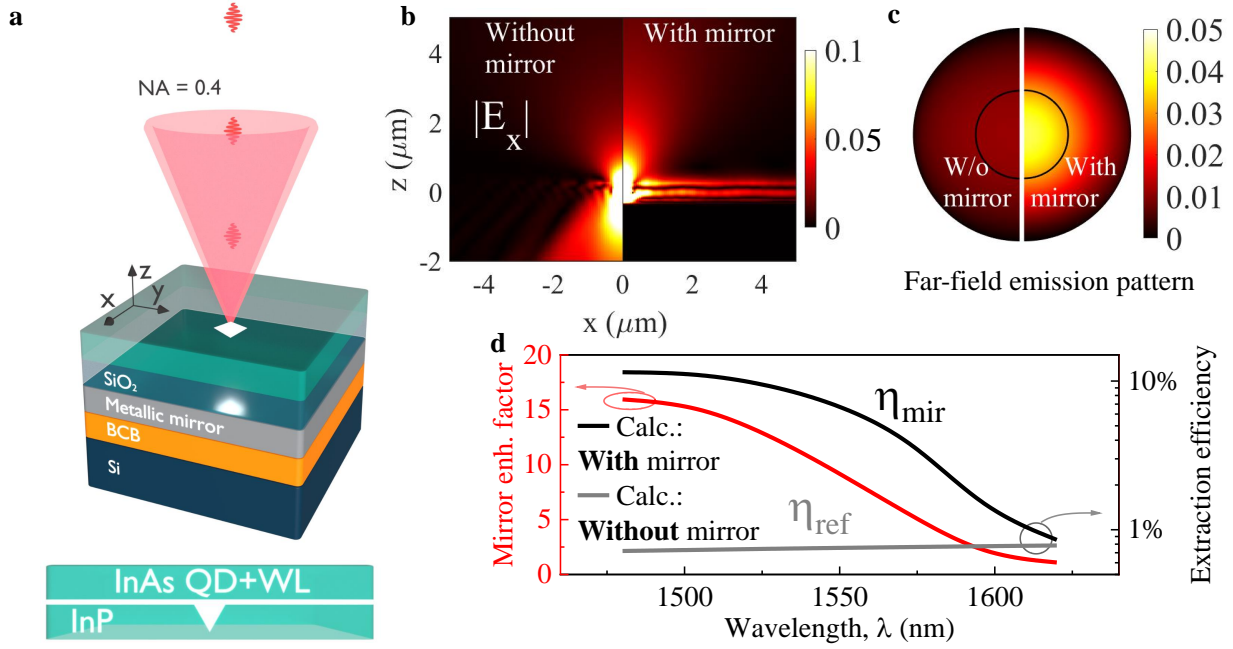


Figure 1. The design of our structures and theoretically estimated performance. **a**, The investigated structure scheme, consisting of InAs/InP quantum dots (QDs) with a metallic reflector integrated on a Si substrate. WL – wetting layer. **b**, The electric field component $|E_x|$ for $\lambda = 1550\text{nm}$ for the structure without (left) and with (right) a metallic reflector made of aluminum (Al). **c**, The calculated far field emission ($P_{\text{ens, NA}}$) for the reference (left) and the device with Al-mirror (right). The half-circle marks the collection cone of a 0.4 NA objective. **d**, The calculated broadband mirror enhancement factor (left axis) and photon extraction efficiency for the QD device with mirror (η_{mir}) and the reference structure without mirror (η_{ref}) as function of emitter wavelength.

The photon extraction efficiency η for as-grown QD-based SPEs is typically $< 1\%$ ¹⁷ due to the large semiconductor-air refractive index contrast, but can be increased by tailoring the local optical environment^{38–40}. Common approaches for increasing η include placing a QD in a monolithic cavity defined by distributed Bragg reflectors (DBRs)³³, in an optical horn structure²⁸, or atop a single DBR reflector^{24,25,31,41}. DBR-based approaches are scalable and η up to 13% was achieved in a narrow spectral window⁴¹, following demanding fabrication in the InAs/InP material system due to layers' low refractive index contrast. With the horn structure, $\eta \approx 11\%$ at 1560 nm (numerical aperture NA=0.55) was shown²⁸, requiring complex fabrication. These approaches however are not suitable for the monolithic integration of QD-based SPEs with Si.

In this work, we propose and demonstrate efficient single photon emission with $\eta > 10\%$ (NA=0.4) and wavelength in the telecom bands. Our photon sources are based on InAs QDs epitaxially grown on InP and heterogeneously integrated on a Si substrate via chemical bonding. We achieve triggered photon emission with a generation purity of $> 98\%$ at a temperature of $T = 4.2\text{K}$ and $\sim 75\%$ at 80K. Further increase of η is possible employing the higher NA objective and tailoring the QD optical environment. Our approach promises localizing individual QDs via optical imaging⁴² and subsequent processing of photonic components with deterministic spatial alignment. Moreover, our QD integration method on the Si-platform provides a broad range of device architecture possibilities, in particular the in-plane emission into planar waveguides as required for on-chip integration.

Results

Structure design

The schematic design of our structures together with calculated device performances are presented in Fig. 1. Self-assembled InAs QDs are placed in a weak planar cavity system formed between a bottom metallic mirror and a top InP/air interface, as illustrated in Fig. 1a. We determine the achievable photon extraction efficiency using numerical simulations of the electromagnetic (EM) field (Fig. 1a) generated by the InAs QD modelled as a classical point dipole with in-plane dipole orientation. The EM field distribution ($|E_x|$) is presented in Fig. 1b for a reference structure without (left panel) and with a metal mirror (right panel). We observe that the effect of the mirror is to suppress leakage of light into the substrate and

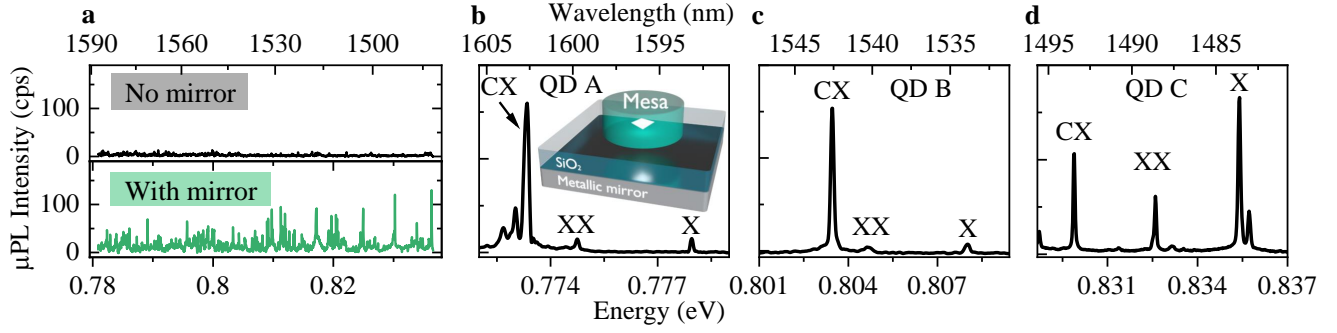


Figure 2. Excitonic complexes in InAs/InP QDs. **a**, Representative high-spatially-resolved photoluminescence (μ PL) spectra recorded for the reference structure without mirror (top panel) and the structure with mirror (bottom panel) with identical pulsed laser excitation at $T = 4.2$ K. **b-d**, μ PL spectra of the investigated InAs/InP QDs (labelled A, B, and C) with identified excitonic emission complexes: neutral exciton (X), biexciton (XX), and charged exciton (CX). Inset to **b**: mesa structure.

instead direct light in the vertical direction. While additional in-plane guiding of light in the slab waveguide formed by the air-semiconductor-metal interfaces is visible, the out-of-plane field pattern is significantly enhanced compared to the structure without reflector. Furthermore, the enhancement is observed in the far field emission pattern presented in Fig. 1c, highlighting the role of the metallic mirror in the directional emission. The black circle represents the collection aperture of a typical, long-working distance microscope objective with a 0.4 NA used for light collection in the experiment, and the extraction efficiency η is then defined as the ratio of the power collected within the NA of the objective ($P_{\text{ens, NA}}$) to the total power emitted by the dipole (Methods. Numerical calculations.). The computed extraction efficiency is presented in Fig. 1d as a function of wavelength. We define the mirror enhancement factor as the ratio between the extraction efficiency for the planar structure with mirror (η_{mir}) and the reference structure (η_{ref}). The presence of the metallic reflector leads to a broadband enhancement of the extraction efficiency (left axis), with the 9.2-fold increase at 1550nm and $\eta \approx 7\%$, and nearly 16-fold increase at 1500nm and $\eta \approx 11\%$. This expected performance is competitive with state-of-the-art extraction efficiencies^{28,41} for single-photon sources operating in the long-wavelength telecom bands.

The device fabrication begins with the epitaxy of an InGaAs sacrificial layer lattice-matched to a standard (001) oriented InP substrate, followed by the growth of an InP λ -cavity with an array of low surface density ($\sim 2.8 \times 10^9 \text{ cm}^{-2}$) InAs QDs placed in the center for quantum confinement (Methods. QD fabrication.). In the next step, the top InP surface is covered by 100 nm of SiO₂ followed by a 100 nm-thick metallic reflector (Al in our case). Subsequently, the chip is flipped and bonded to a Si substrate using benzocyclobutene (BCB) and finally, the thick InP substrate, now on top, and the InGaAs sacrificial layer are removed (Methods. QD integration with Si substrate.). We emphasize that this approach and the dimensions are suitable for in-plane photon emission into a Si photonic circuit, although not explicitly pursued in this work. We applied a two-fold experimental evaluation strategy to verify the significant robustness of the structure design with respect to the level of η and the related broadband performance, and to present bright SPEs heterogeneously integrated on a Si substrate. In Figure 2a, we present emission spectra obtained from a reference structure without metallic reflector and the planar structure containing the metallic mirror, both recorded with the same high spatial resolution photoluminescence setup (μ PL) from a diffraction limited spot (Methods. Optical experiments.). The spectra consist of multiple sharp emission lines distributed over a broad spectral range, originating from QDs of mainly different sizes within the optical excitation spot and various emission complexes including neutral exciton (X), charged exciton (CX), and biexciton (XX) transitions. For the structure containing the mirror and compared to the reference structure, we observe a clear intensity enhancement of the emission lines.

The quantitative analysis of photon extraction efficiency η from SPEs requires the isolation of single QDs and identification of their respective spectral features. We therefore proceeded with the processing of the mirror-containing planar structure to fabricate cylindrical mesas with diameters of $D_1 = 2 \mu\text{m}$ and $D_2 = 3 \mu\text{m}$, respectively, as schematically illustrated in the inset of Fig. 2b. The finite size of the mesas allows for the spatial isolation of single QDs, a vital element in single-photon source engineering, and leads to modifications of the calculated EM field pattern and extraction efficiencies (see Supplementary Figure S3).

In Figures 2b-2d, we present the μ PL spectra of three representative and isolated QD emitters, which in the following we refer to as QD A, B, and C, with their emission spectrum located in the telecom L-, C-, and S-band, respectively. The indicated excitonic complexes (X, CX, XX) are identified based on a series of excitation-power-dependent and polarization-resolved μ PL measurements (see Supplementary Figure S1), and confirmed by the cross-correlation of the XX-X and CX-X complexes.

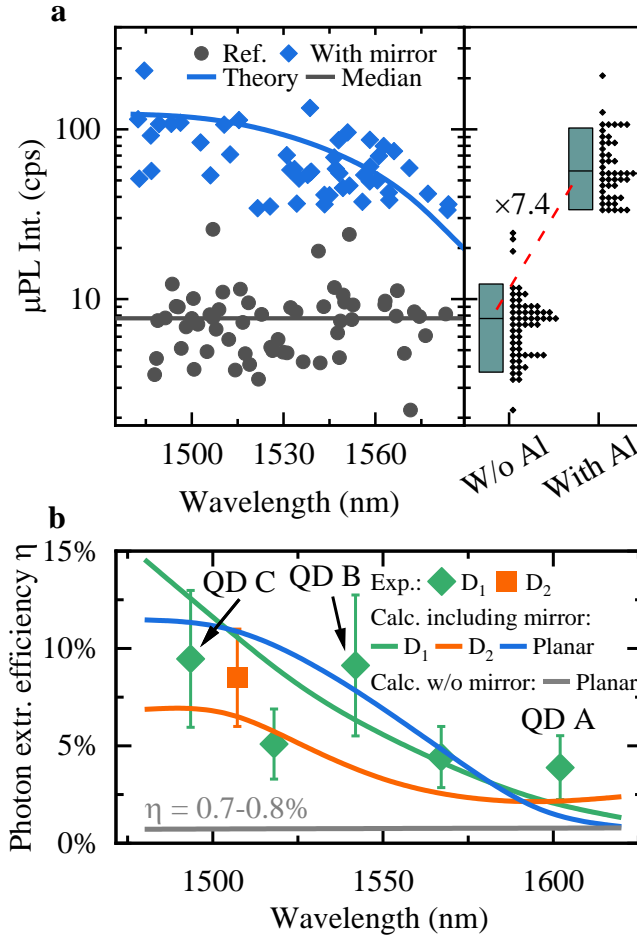


Figure 3. Photon extraction efficiency for the investigated structures. **a**, Left panel: comparison of the μ PL intensity of ~ 50 brightest emission lines (points) for the planar mirror-containing (blue diamonds) and the reference (black circles) structures, respectively. The solid blue line is the expected μ PL intensity for mirror-containing structure obtained by multiplying the median μ PL intensity of the reference structure (solid black line) by the mirror enhancement factor (cf. red line in Fig. 1d). Right panel: statistical analysis of measured intensities. Boxes illustrate one standard deviation, the line inside the box is the median value of each distribution shown as points. **b**, Photon extraction efficiency η for the mesa-processed structure with a metallic mirror. Green diamonds show recorded η values for mesas with $D_1 = 2\ \mu\text{m}$ including QDs A-C. The result shown as orange square is obtained for an emitter in a mesa with $D_2 = 3\ \mu\text{m}$. The solid lines represent calculated η values obtained with the modal method for mesas with $D_1 = 2\ \mu\text{m}$ (green) and $D_2 = 3\ \mu\text{m}$ (orange). Solid blue and grey lines show the calculated η for a planar structure with mirror and a reference structure without mirror, respectively.

(see Supplementary Figure S2).

Brightness of SPEs

We employ two approaches to compare the calculated with the experimentally obtained photon extraction efficiency η . In the first approach, we consider the broadband enhancement of the photon extraction for planar structures due to the mirror. The approach is based on the statistical analysis of correlated and uncorrelated emission processes, from where we derive a rough estimate of η . We thus compare the intensity of nearly 50 spectral lines recorded from the mirror-containing and the reference structure, respectively, and the results are plotted in Fig. 3a. The spectrally averaged enhancement factor of $7.4^{+1.6}_{-1.3}$ is obtained by comparing the median values for the distributions of emission intensity, which can be converted to a mean photon extraction efficiency $\eta \approx 6\%$ for the device containing the metallic mirror. The 95% confidence levels for the enhancement factor are calculated according to Ref.⁴³. In the second approach, we adopt the method described by M. Gschrey et al.⁴⁴ and directly measure η for individual QDs in mesa-processed structures. The results for η from in total 6

QDs (including QDs A-C) are presented in Fig. 3b together with the numerically calculated values. For these mesa structures, we experimentally determine photon extraction efficiencies η above 4.4%, and as high as $\eta_B = 9.1\%$ and $\eta_C = 9.5\%$ for QDs B and C, respectively. Those values demonstrate a one order of magnitude improvement compared to the efficiency 0.7-0.8% estimated for the reference structure without the metallic mirror. Importantly, we obtain good agreement between the experimentally determined extraction efficiency and the theoretical prediction, both for the broadband approach (Fig. 3a) and the individually investigated 6 QDs in mesas (Fig. 3b). We attribute the small deviations between simulation and experimental values to possible non-radiative recombination channels in the QD vicinity, changes in the mesa geometry due to fabrication imperfections and non-deterministic positioning of the QD within the mesa. While these effects generally result in a lower recorded photon flux compared to the theoretical prediction, we note that a ~ 200 nm displacement of a QD from the mesa center results in an increase in the extraction efficiency as compared to a QD placed in the center. Such a displacement may explain the high η value obtained for QD B (see Supplementary Figure S3 for further details).

Evaluation of the photon purity

The order of magnitude improvement in photon extraction efficiency from InAs/InP QDs renders our structures an attractive source of single photons heterogeneously integrated with the Si-platform. We evaluate in the following the quality of single-photon emission from the QDs in mesa structures by investigating the purity of single photons emitted from QDs A-C. For that purpose, we recorded the second-order correlation function $g^{(2)}(\tau)$ exploiting off-resonant continuous wave (cw) and pulsed excitation schemes (Methods. Optical experiments.), and the obtained histograms without normalization are presented in Figure 4. For pulsed excitation (Fig. 4a), we observe that the coincidences $\tau \approx 0$ are strongly suppressed compared to the coincidence peaks at multiples of the inverse laser repetition rate ($\tau_0 = 25$ ns). Furthermore, we record a significant dip in the histogram counts at short time delays $|\tau| < 5$ ns (insets to Fig. 4a). This feature indicates the capture of more than one carrier by the QD and cascaded photon emission within a single excitation, effectively resulting in multi-photon events⁴⁵ within $|\tau| < 5$ ns. We explain this observation with the off-resonant excitation scheme applied in our experiment, where a substantial amount of carriers are excited and trapped in the wetting layer or in other charge trap states⁴⁵⁻⁴⁷. After release, those carriers are captured by the QD within the characteristic capture time τ_{cap} and produce secondary photons⁴⁸ via exciton recombination with the time constant τ_{dec} .

We fit the correlation histograms obtained with pulsed laser excitation with the function^{29,49}:

$$C(\tau) = B + A \left[\exp(-|\tau|/\tau_{\text{dec}}) - \exp(-|\tau|/\tau_{\text{cap}}) \right] + H \sum_{n \neq 0} \exp(-|\tau - n\tau_0|/\tau_{\text{dec}}), \quad (1)$$

where B is the level of background coincidences, A is a scaling parameter related to secondary photon emission, $n \neq 0$ the peak number and H the average height of the peaks at $\tau_n = n\tau_0$. The second-order correlation function $g^{(2)}(\tau)$ is then obtained by normalizing $C(\tau)$ with H , and all fit parameters are summarized in Supplementary Table S2. Evaluating $g^{(2)}(\tau)$ at $\tau = 0$, we obtain a single photon emission purity $\mathcal{P} = 1 - g^{(2)}(\tau = 0)$ of $97.7 \pm 1.0\%$, $91.3 \pm 1.7\%$, and $98.2 \pm 1.2\%$ for QDs A-C, respectively. This estimation ignores coincidences produced by secondary photon emission events which may be avoided asymptotically employing an on-resonance excitation scheme. Comparing the integrated peak area of $g^{(2)}(\tau = 0)$ with the average peak area at τ_n , as it is relevant for applications of our single photon sources in QIP, yields values for $\mathcal{P}_{\text{area}}$ of $62.9 \pm 2.0\%$, $56.7 \pm 1.8\%$, and $79.5 \pm 2.0\%$ for QDs A-C, respectively (see Methods). We also correct the emission purity $\mathcal{P}_{\text{area,cor}}$ for background coincidences B and obtain values of $72.4 \pm 2.0\%$, $79.1 \pm 1.8\%$, and $88.6 \pm 2.0\%$ for QDs A-C. The emission purity recorded in the pulsed regime is mainly limited by the capture of secondary carriers and subsequent photon emission. We note that the data is well described by our model and does not consider the capture of secondary carriers at τ_n . Furthermore, with the modelling routine we determine τ_{dec} in the range 1.9-2.8 ns, which is in accordance with the CX decay time measured in time-resolved μ PL (see Supplementary Figure S4).

Importantly, the obtained single photon purity of the investigated structures is very robust for a wide range of temperatures and excitation powers. In Figs. 4b-4c we present correlation histograms recorded in CW excitation mode from the CX line of QD B at sample temperatures of 4 K and 80 K, respectively, while optically pumping at the saturation power P_{sat} (see Supplementary Figure S5 for correlation histograms taken at $T = 30$ K, $T = 50$ K, at $0.3 \times P_{\text{sat}}$, $0.7 \times P_{\text{sat}}$, and Supplementary Table S4 for the obtained $g^{(2)}(0)$ values). At 80 K sample temperature, which easily can be reached with a liquid nitrogen dewar or a cryogen-free Stirling cooler²⁷, a significant feature at $\tau = 0$ is visible in the histogram, quantifying the robustness of this source of single photons. We fitted the normalized histograms recorded in cw mode with a standard single-exponential function⁵⁰ (see Methods) to extract the single photon emission purity from the measurements. The raw data estimated purity from the histogram recorded at P_{sat} is $\mathcal{P}_{\text{raw}} = (97.3 \pm 2.7\%)$ (see Methods) limited by the finite time resolution of our setup. The best fit to our data thus suggests even higher values of photon purity ($\mathcal{P} = 100\%$), with a standard error $\sigma = 0.038$, and without background correction. Such high-purity of the single-photon flux in the high-excitation power regime ($P \geq P_{\text{sat}}$) has previously been observed only for InAs/GaAs QDs emitting at $\lambda = (910 \text{ nm} - 920 \text{ nm})$ ^{38,51}. In contrast to these sources, the structure

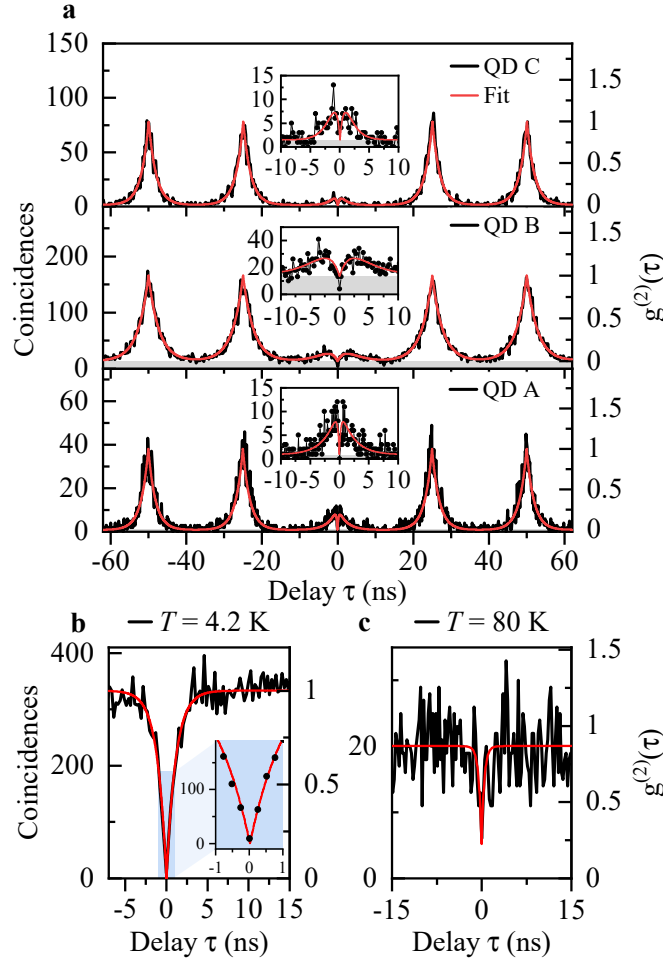


Figure 4. Autocorrelation histograms for CX lines. **a**, Triggered single-photon emission for investigated QDs: C (top), B (center), A (bottom). Insets: Close-ups of the histograms showing coincidences around zero delay. **b**, **c**, Single-photon emission under cw excitation for the CX in QD B, recorded **b** under the laser excitation power corresponding to the saturation of the CX μ PL intensity (inset: zoom around $\tau = 0$), and **c** at $T = 80$ K. Red lines are fits to the experimental data. Grey area in **a** shows the level of background coincidences B obtained by the fit with Eq. (1).

investigated here demonstrates high brightness and close-to-ideal single-photon purity while emitting in the telecom C-band. Increasing the temperature to $T = 80$ K, leads to a reduction of the emission line visibility (see Supplementary Figure S6 for the analysis of temperature-dependent μ PL of QD B), yet we obtain a relatively high purity of single photon emission with the fitted value of $\mathcal{P}_{80\text{K}} = 0.75$ ($\sigma = 0.19$, without background correction). We note that the achieved purity at $T = 80$ K is higher than the record values of $g^{(2)}(0) = 0.34$ and $g^{(2)}(0) = 0.33$ previously reported at this temperature and at $1.55 \mu\text{m}$ emission wavelength achieved with InAs/InAlGaAs/InP quantum dashes^{18,52} and InAs/GaAs QDs grown with the metamorphic approach⁵³, respectively. Importantly, both these previous approaches are obtained in different carrier confinement conditions, InAlGaAs or GaAs barriers respectively, and thus cannot be directly compared with the pure InAs/InP system investigated here.

Discussion

The demonstrated design of the structure with InAs/InP QDs on a metallic mirror integrated on a Si substrate paves the way towards a simplified, small-footprint, cost-effective, and scalable manufacturing process of triggered single-photon emitters operating in the telecom S-, C-, and L-bands, suitable for Si-based on-chip photonic quantum information processing. The spectral range of the InAs/InP single-photon emitters investigated here eliminates the necessity for frequency conversion to the telecom bands, potentially allowing for the implementation of distributed schemes for information processing and computation using low-loss fiber-based optical networks. Combining the robust design of our structures and the manufacturing process compatible with the existing industry standards establishes single-photon sources with high photon extraction efficiency in the

broader telecom spectral range, with performance properties comparable to the DBR based solutions but with significantly reduced fabrication related technological demands.

The presented robust architecture, offering spectrally broad high photon extraction efficiency, is beneficial for further processing steps tailoring photonic environment of a deterministically localized emitter. The emitter high brightness allows for its fast spatial positioning utilizing the emission imaging method successfully employed for short-wavelength (< 1000 nm) QDs⁴². However, at telecom wavelengths, the imaging relies on a 2D state-of-the-art InGaAs-based matrices with yet poor efficiencies and high noise levels compared to Si-based arrays desired for shorter wavelengths. Therefore, the simplified architecture of a QD on a metal mirror can open the route towards fabrication of fully deterministic, scalable QPICs at telecom wavelengths.

Methods

QD fabrication

The QDs are grown in the low-pressure MOVPE TurboDisc® reactor using arsine (AsH₃), phosphine (PH₃), tertiarybutylphosphine (TBP) and trimethylindium (TMIn) precursors with H₂ as a carrier gas. The growth sequence starts with the deposition of a 0.5 μm-thick InP buffer layer on a (001)-oriented InP substrate at 610 °C subsequently epitaxially covered by a 200 nm-thick In_{0.53}Ga_{0.47}As sacrificial layer lattice-matched to InP and a 244 nm-thick InP layer. Then, the temperature is decreased to 483 °C, stabilized under TBP for 180 s and AsH₃ for 27 s. Finally, nucleation of QDs occurs in the Stranski-Krastanov growth mode after deposition of nominally 0.93 mono-layer thick InAs under TMIn and AsH₃ flow rates of 11.8 μmol/min and 52.2 μmol/min, respectively. Nucleated QDs are annealed for 60 s at the growth temperature in AsH₃ ambient, before the temperature is increased for 30 s to 515 °C and the annealing continues for another 30 s. Deposition of a 244 nm-thick InP capping layer (12 nm at 515 °C, and the remaining 232 nm after increasing the temperature up to 610 °C) finishes the growth sequence.

QD integration on Si substrate

To integrate the QD structure on Si, a 100 nm-thick layer of SiO₂ is deposited on top of the InP-based structure using plasma-enhanced chemical vapor deposition (PECVD) with the rate of 0.99 nm/s, and subsequently covered by a 100 nm-thick Al layer deposited via electron-beam evaporation with the rate of 90 Å/s. After flipping the structure bottom-up, it is bonded to the Si substrate. The bonding procedure includes, first, spin coating of the AP3000 adhesion promoter and benzocyclobutene (BCB) on Si and AP3000 on the InP wafer, and second, both structures are bonded at 250 °C in vacuum under an applied force of ~ 2 kN. Plasma ashing disposes superfluous BCB from the back-side of the InP wafer. Afterward, the InP substrate is removed in HCl and the InGaAs etch stop layer in H₂SO₄:H₂O₂:H₂O=1:8:80 mixture. For the sample with mesas, HSQ resist (a high purity silsesquioxane-based semiconductor grade polymer) is spin-coated and exposed using electron-beam lithography and developed in water-diluted AZ400K. The mesa pattern is then transferred to the InP by inductively coupled plasma-reactive ion etching (ICP-RIE) followed by HSQ removal in a buffered oxide etch (BHF). The mesa height is 300 nm as measured with an atomic force microscope.

Optical experiments

For the optical experiments, the structure is held in a helium-flow cryostat allowing for controlled sample temperatures in the range of 4.2 K to 300 K. For our standard μPL studies, the structures are optically excited through a high numerical aperture (NA = 0.4) microscope objective with 20× magnification with 660 nm or 787 nm light generated with semiconductor laser diodes, respectively. The same objective is used to collect the PL and direct it for spectral analysis to a 1 m-focal-length monochromator equipped with a liquid-nitrogen-cooled InGaAs multichannel array detector, providing spatial and spectral resolution of ≈ 2 μm and ≈ 25 μeV, respectively. Polarization properties of emitted light are analyzed by rotating a half-wave plate mounted before a fixed high-contrast-ratio (10⁶:1) linear polarizer, both placed in front of the monochromator entrance.

Autocorrelation histograms, photon extraction efficiency, and TRPL are measured in a similar setup. In this setup, the structures are excited by a train of ~ 50 ps-long pulses with a repetition frequency of 40 MHz or 80 MHz, and the central photon wavelength of 805 nm. The collected photons are dispersed by a 0.32 m-focal-length monochromator equipped either with a InGaAs multichannel array detector or NbN-based superconducting nanowire single-photon detectors (SNSPDs) with ~90 % quantum efficiency in the 1.5 μm to 1.6 μm range and ~ 200 dark counts per second. A multichannel picosecond event timer analyzes the single photon counts as time-to-amplitude converter with 256 ps channel time bin width. The overall time resolution of the setup is ~80 ps.

Determination of the photon extraction efficiency

To determine the value of photon extraction efficiency η_{QD} , we follow the method described in Ref.⁵¹. First, we estimate the efficiency of the setup η_{Setup} by reflecting a laser tuned to the investigated QD emission range off a silver mirror placed in the

setup instead of the structure. The laser beam is attenuated with neutral density filters to achieve the SNSPD count rate in the MHz range. This number is corrected by the measured mirror reflectivity, attenuation of filters, transmission of the cryostat window and the microscope objective. Based on the laser power, the estimated setup efficiency is $\eta_{\text{Setup}} = (0.18 \pm 0.06) \%$, with the uncertainty being the standard deviation $\sigma(\eta)$ of $\eta_{\text{Setup}}(\lambda)$, mainly stemming from the slight discrepancies in the fiber in-coupling efficiencies for different wavelengths. Then, we excite the QDs non-resonantly with a pulsed laser diode with $f_{\text{rep}} = 80\text{MHz}$ repetition rate at the saturation power for each QD. We collect the emission with the microscope objective (NA = 0.4), sum the SNSPD count rates for CX and X lines (n_{QD}), as only one excitonic complex can radiatively decay at a time, and correct them by η_{Setup} . Taking into account the laser repetition f , we estimate the photon extraction efficiency $\eta_{\text{QD}} = n_{\text{QD}}/(f \times \eta_{\text{Setup}})$. The error bars for photon extraction efficiencies are calculated by propagating the $\sigma(\eta)$ uncertainty. This method assumes unity internal quantum efficiency of QDs ($\eta_{\text{int}} = 100\%$), respectively the QD photon repetition rate equals f_{rep} . It is however difficult to determine experimentally the contribution of non-radiative recombination and hence the real value of η_{int} . The assumption of $\eta_{\text{int}} = 100\%$ thus determines a lower limit of η_{QD} due to a possible overestimation of the total number of photons emitted by the QD (n_{QD}). Finally, we correct the measured η values for the QDs A-C by the factor $\sqrt{1 - g^{(2)}(0)_{\text{area}}}$ to account for the secondary photons due to the refilling of QD states that contribute to the measured photon flux^{47,54}. This procedure only slightly reduces the η values by 16%, 11%, and 5% for QDs A, B, and C, respectively. With this correction, the highest η values are 9.5% and 9.1% for QDs C and B, respectively.

Determining the single-photon purity

For the pulsed QD excitation, we calculate the $g^{(2)}(0)$ value including the histogram background contribution B :

$$g^{(2)}(0)_{\text{area}} = \int_{-T_0/2}^{T_0/2} [B + A [\exp(-|\tau|/\tau_{\text{dec}}) - \exp(-|\tau|/\tau_{\text{cap}})]] d\tau / \int_{-T_0/2}^{T_0/2} [B + H \exp(-|\tau|/\tau_{\text{dec}})] d\tau, \quad (2)$$

and with the background contribution subtracted:

$$g^{(2)}(0)_{\text{area}} = \int_{-T_0/2}^{T_0/2} A [\exp(-|\tau|/\tau_{\text{dec}}) - \exp(-|\tau|/\tau_{\text{cap}})] d\tau / \int_{-T_0/2}^{T_0/2} H \exp(-|\tau|/\tau_{\text{dec}}) d\tau. \quad (3)$$

For the histograms recorded in cw mode we use the standard equation $C(\tau) = N [1 - (1 - g_{\text{fit}}^{(2)}(0)) \exp(-|\tau|/t_r)]$, where N is the average coincidence level at $|\tau| \gg 0$. The purity is extracted as $\mathcal{P} = 1 - g^{(2)}(0)$, in particular, for the raw-data estimated purity $\mathcal{P}_{\text{raw}} = C(0)/N$.

Numerical calculations

The structure is modeled with a modal method (MM) employing a true open geometry boundary condition⁵⁵. Here, the geometry is divided into uniform layers along a propagation z axis, and the field is expanded on eigenmodes of each uniform layer. The eigenmode expansion coefficients in the QD layer are computed using the reciprocity theorem⁵⁶, and the fields are connected at each layer interface using the S matrix formalism^{56,57}. The far field is then determined using the field equivalence principle and radiation integrals⁵⁸. The extraction efficiency is defined as $\eta = P_{\text{ens, NA}}/P_{\text{in}}$, where $P_{\text{ens, NA}}$ is the power detected by the lens with NA = 0.4 in the far field, and P_{in} is the total power emitted from the dipole.

References

1. Knill, E., Laflamme, R. & Milburn, G. J. A scheme for efficient quantum computation with linear optics. *Nature* **409**, 46–52, DOI: [10.1038/35051009](https://doi.org/10.1038/35051009) (2001).
2. Kok, P. *et al.* Linear optical quantum computing with photonic qubits. *Rev. Mod. Phys.* **79**, 135–174, DOI: [10.1103/RevModPhys.79.135](https://doi.org/10.1103/RevModPhys.79.135) (2007).
3. Wang, Z. M. *et al.* Boson Sampling with 20 Input Photons and a 60-Mode Interferometer in a 1014 -Dimensional Hilbert Space. *Phys. Rev. Lett.* **123**, 250503, DOI: [10.1103/PhysRevLett.123.250503](https://doi.org/10.1103/PhysRevLett.123.250503) (2019).
4. Elshaari, A. W., Pernice, W., Srinivasan, K., Benson, O. & Zwiller, V. Hybrid integrated quantum photonic circuits. *Nat. Photonics* **14**, 285–298, DOI: [10.1038/s41566-020-0609-x](https://doi.org/10.1038/s41566-020-0609-x) (2020).
5. Zhong, H.-S. *et al.* Quantum computational advantage using photons. *Science* **370**, 1460–1463, DOI: [10.1126/science.abe8770](https://doi.org/10.1126/science.abe8770) (2020). <https://science.sciencemag.org/content/370/6523/1460.full.pdf>.
6. Shalm, L. K. *et al.* Strong loophole-free test of local realism. *Phys. Rev. Lett.* **115**, 250402, DOI: [10.1103/PhysRevLett.115.250402](https://doi.org/10.1103/PhysRevLett.115.250402) (2015).

7. Giustina, M. *et al.* Significant-loop-hole-free test of bell's theorem with entangled photons. *Phys. Rev. Lett.* **115**, 250401, DOI: [10.1103/PhysRevLett.115.250401](https://doi.org/10.1103/PhysRevLett.115.250401) (2015).
8. Takemoto, K. *et al.* Quantum key distribution over 120 km using ultrahigh purity single-photon source and superconducting single-photon detectors. *Sci. Rep.* **5**, 14383, DOI: [10.1038/srep14383](https://doi.org/10.1038/srep14383) (2015).
9. Yin, J. *et al.* Entanglement-based secure quantum cryptography over 1,120 kilometres. *Nature* **582**, 501–505, DOI: [10.1038/s41586-020-2401-y](https://doi.org/10.1038/s41586-020-2401-y) (2020).
10. Wang, J., Sciarrino, F., Laing, A. & Thompson, M. G. Integrated photonic quantum technologies. *Nat. Photonics* **14**, 273–284, DOI: [10.1038/s41566-019-0532-1](https://doi.org/10.1038/s41566-019-0532-1) (2019).
11. Wang, J. *et al.* Multidimensional quantum entanglement with large-scale integrated optics. *Science* **360**, 285–291, DOI: [10.1126/science.aar7053](https://doi.org/10.1126/science.aar7053) (2018).
12. Qiang, X. *et al.* Large-scale silicon quantum photonics implementing arbitrary two-qubit processing. *Nat. Photonics* **12**, 534–539 (2018).
13. Paesani, S. *et al.* Generation and sampling of quantum states of light in a silicon chip. *Nat. Phys.* **15**, 925–929, DOI: [10.1038/s41567-019-0567-8](https://doi.org/10.1038/s41567-019-0567-8) (2019).
14. Kim, J.-H. *et al.* Hybrid integration of solid-state quantum emitters on a silicon photonic chip. *Nano Lett.* **17**, 7394–7400, DOI: [10.1021/acs.nanolett.7b03220](https://doi.org/10.1021/acs.nanolett.7b03220) (2017).
15. Eisaman, M. D., Fan, J., Migdall, A. & Polyakov, S. V. Invited review article: Single-photon sources and detectors. *Rev. Sci. Instruments* **82**, 071101, DOI: [10.1063/1.3610677](https://doi.org/10.1063/1.3610677) (2011).
16. Aharonovich, I., Englund, D. & Toth, M. Solid-state single-photon emitters. *Nat. Photonics* **10**, 631–641, DOI: [10.1038/nphoton.2016.186](https://doi.org/10.1038/nphoton.2016.186) (2016).
17. Senellart, P., Solomon, G. & White, A. High-performance semiconductor quantum-dot single-photon sources. *Nat. Nanotechnol.* **12**, 1026–1039, DOI: [10.1038/nnano.2017.218](https://doi.org/10.1038/nnano.2017.218) (2017).
18. Arakawa, Y. & Holmes, M. J. Progress in quantum-dot single photon sources for quantum information technologies: A broad spectrum overview. *Appl. Phys. Rev.* **7**, 021309, DOI: [10.1063/5.0010193](https://doi.org/10.1063/5.0010193) (2020).
19. Tran, M. A. *et al.* Ultra-Low-Loss Silicon Waveguides for Heterogeneously Integrated Silicon/III-V Photonics. *Appl. Sci.* **8**, 1139, DOI: [10.3390/app8071139](https://doi.org/10.3390/app8071139) (2018).
20. Vlasov, Y. A. & McNab, S. J. Losses in single-mode silicon-on-insulator strip waveguides and bends. *Opt. Express* **12**, 1622, DOI: [10.1364/opex.12.001622](https://doi.org/10.1364/opex.12.001622) (2004).
21. Wehner, S., Elkouss, D. & Hanson, R. Quantum internet: A vision for the road ahead. *Science* **362**, eaam9288, DOI: [10.1126/science.aam9288](https://doi.org/10.1126/science.aam9288) (2018).
22. Cuomo, D., Caleffi, M. & Cacciapuoti, A. S. Towards a distributed quantum computing ecosystem. *IET Quantum Commun.* **1**, 3–8, DOI: [10.1049/iet-qt.2020.0002](https://doi.org/10.1049/iet-qt.2020.0002) (2020).
23. Semenova, E. S. *et al.* Metamorphic approach to single quantum dot emission at 1.55 μm on GaAs substrate. *J. Appl. Phys.* **103**, 103533, DOI: [10.1063/1.2927496](https://doi.org/10.1063/1.2927496) (2008).
24. Paul, M. *et al.* Single-photon emission at 1.55 μm from MOVPE-grown InAs quantum dots on InGaAs/GaAs metamorphic buffers. *Appl. Phys. Lett.* **111**, 033102, DOI: [10.1063/1.4993935](https://doi.org/10.1063/1.4993935) (2017).
25. Zeuner, K. D. *et al.* On-demand generation of entangled photon pairs in the telecom C-band for fiber-based quantum networks (2019). ArXiv, [1912.04782](https://arxiv.org/abs/1912.04782).
26. Nawrath, C. *et al.* Coherence and indistinguishability of highly pure single photons from non-resonantly and resonantly excited telecom C-band quantum dots. *Appl. Phys. Lett.* **115**, 023103, DOI: [10.1063/1.5095196](https://doi.org/10.1063/1.5095196) (2019).
27. Musiał, A. *et al.* Plug&Play Fiber-Coupled 73 kHz Single-Photon Source Operating in the Telecom O-Band. *Adv. Quantum Technol.* **3**, 2000018, DOI: [10.1002/qute.202000018](https://doi.org/10.1002/qute.202000018) (2020).
28. Takemoto, K. *et al.* An optical horn structure for single-photon source using quantum dots at telecommunication wavelength. *J. Appl. Phys.* **101**, 081720, DOI: [10.1063/1.2723177](https://doi.org/10.1063/1.2723177) (2007).
29. Miyazawa, T. *et al.* Single-photon emission at 1.5 μm from an InAs/InP quantum dot with highly suppressed multi-photon emission probabilities. *Appl. Phys. Lett.* **109**, 132106, DOI: [10.1063/1.4961888](https://doi.org/10.1063/1.4961888) (2016).
30. Birowosuto, M. D. *et al.* Fast Purcell-enhanced single photon source in 1,550-nm telecom band from a resonant quantum dot-cavity coupling. *Sci. Rep.* **2**, 321, DOI: [10.1038/srep00321](https://doi.org/10.1038/srep00321) (2012).

31. Benyoucef, M., Yacob, M., Reithmaier, J. P., Kettler, J. & Michler, P. Telecom-wavelength (1.5 μm) single-photon emission from InP-based quantum dots. *Appl. Phys. Lett.* **103**, 162101, DOI: [10.1063/1.4825106](https://doi.org/10.1063/1.4825106) (2013).
32. Skiba-Szymanska, J. *et al.* Universal growth scheme for quantum dots with low fine-structure splitting at various emission wavelengths. *Phys. Rev. Appl.* **8**, 014013, DOI: [10.1103/physrevapplied.8.014013](https://doi.org/10.1103/physrevapplied.8.014013) (2017).
33. Müller, T. *et al.* A quantum light-emitting diode for the standard telecom window around 1,550 nm. *Nat. Commun.* **9**, 862, DOI: [10.1038/s41467-018-03251-7](https://doi.org/10.1038/s41467-018-03251-7) (2018).
34. Anderson, M. *et al.* Quantum teleportation using highly coherent emission from telecom C-band quantum dots. *npj Quantum Inf.* **6**, 14, DOI: [10.1038/s41534-020-0249-5](https://doi.org/10.1038/s41534-020-0249-5) (2020).
35. Anderson, M. *et al.* Gigahertz-Clocked Teleportation of Time-Bin Qubits with a Quantum Dot in the Telecommunication C Band. *Phys. Rev. Appl.* **13**, 1, DOI: [10.1103/PhysRevApplied.13.054052](https://doi.org/10.1103/PhysRevApplied.13.054052) (2020).
36. Holewa, P. *et al.* Optical and electronic properties of low-density InAs/InP quantum-dot-like structures designed for single-photon emitters at telecom wavelengths. *Phys. Rev. B* **101**, 195304, DOI: [10.1103/PhysRevB.101.195304](https://doi.org/10.1103/PhysRevB.101.195304) (2020).
37. Cao, X., Zopf, M. & Ding, F. Telecom wavelength single photon sources. *J. Semicond.* **40**, 071901, DOI: [10.1088/1674-4926/40/7/071901](https://doi.org/10.1088/1674-4926/40/7/071901) (2019).
38. Claudon, J. *et al.* A highly efficient single-photon source based on a quantum dot in a photonic nanowire. *Nat. Photonics* **4**, 174–177, DOI: [10.1038/nphoton.2009.287x](https://doi.org/10.1038/nphoton.2009.287x) (2010).
39. Stepanov, P. *et al.* Highly directive and gaussian far-field emission from “giant” photonic trumpets. *Appl. Phys. Lett.* **107**, 141106, DOI: [10.1063/1.4932574](https://doi.org/10.1063/1.4932574) (2015).
40. Liu, J. *et al.* A solid-state source of strongly entangled photon pairs with high brightness and indistinguishability. *Nat. Nanotechnol.* **14**, 586–593, DOI: [10.1038/s41565-019-0435-9](https://doi.org/10.1038/s41565-019-0435-9) (2019).
41. Musiał, A. *et al.* InP-based single-photon sources operating at telecom C-band with increased extraction efficiency. *Appl. Phys. Lett.* **118**, 221101, DOI: [10.1063/5.0045997](https://doi.org/10.1063/5.0045997) (2021).
42. Sapienza, L., Davanço, M., Badolato, A. & Srinivasan, K. Nanoscale optical positioning of single quantum dots for bright and pure single-photon emission. *Nat. Commun.* **6**, 7833, DOI: [10.1038/ncomms8833](https://doi.org/10.1038/ncomms8833) (2015).
43. Bonett, D. G. & Price, R. M. Confidence Intervals for Ratios of Means and Medians. *J. Educ. Behav. Stat.* **45**, 750–770, DOI: [10.3102/1076998620934125](https://doi.org/10.3102/1076998620934125) (2020).
44. Gschrey, M. *et al.* In situ electron-beam lithography of deterministic single-quantum-dot mesa-structures using low-temperature cathodoluminescence spectroscopy. *Appl. Phys. Lett.* **102**, 251113, DOI: [10.1063/1.4812343](https://doi.org/10.1063/1.4812343) (2013).
45. Fischbach, S. *et al.* Single quantum dot with microlens and 3D-printed micro-objective as integrated bright single-photon source. *ACS Photonics* **4**, 1327–1332, DOI: [10.1021/acsp Photonics.7b00253](https://doi.org/10.1021/acsp Photonics.7b00253) (2017).
46. Peter, E. *et al.* Fast radiative quantum dots: From single to multiple photon emission. *Appl. Phys. Lett.* **90**, 223118, DOI: [10.1063/1.2744475](https://doi.org/10.1063/1.2744475) (2007).
47. Kumano, H. *et al.* Stable and efficient collection of single photons emitted from a semiconductor quantum dot into a single-mode optical fiber. *Appl. Phys. Express* **9**, 032801, DOI: [10.7567/apex.9.032801](https://doi.org/10.7567/apex.9.032801) (2016).
48. Chang, H.-S. *et al.* Origins of nonzero multiple photon emission probability from single quantum dots embedded in photonic crystal nanocavities. *Appl. Phys. Lett.* **94**, 163111, DOI: [10.1063/1.3125222](https://doi.org/10.1063/1.3125222) (2009).
49. Dalgarno, P. A. *et al.* Hole recapture limited single photon generation from a single n-type charge-tunable quantum dot. *Appl. Phys. Lett.* **92**, 193103, DOI: [10.1063/1.2924315](https://doi.org/10.1063/1.2924315) (2008).
50. Michler, P. *et al.* Quantum correlation among photons from a single quantum dot at room temperature. *Nature* **406**, 968, DOI: [10.1038/35023100](https://doi.org/10.1038/35023100) (2000).
51. Gschrey, M. *et al.* Highly indistinguishable photons from deterministic quantum-dot microlenses utilizing three-dimensional in situ electron-beam lithography. *Nat. Commun.* **6**, 7662, DOI: [10.1038/ncomms8662](https://doi.org/10.1038/ncomms8662) (2015).
52. Dusanowski, Ł. *et al.* Single-photon emission of InAs/InP quantum dashes at 1.55 μm and temperatures up to 80 K. *Appl. Phys. Lett.* **108**, 163108, DOI: [10.1063/1.4947448](https://doi.org/10.1063/1.4947448) (2016).
53. Carmesin, C. *et al.* Structural and optical properties of InAs/(In)GaAs/GaAs quantum dots with single-photon emission in the telecom C-band up to 77 K. *Phys. Rev. B* **98**, 125407, DOI: [10.1103/PhysRevB.98.125407](https://doi.org/10.1103/PhysRevB.98.125407) (2018).
54. Yang, J. *et al.* Quantum dot-based broadband optical antenna for efficient extraction of single photons in the telecom O-band. *Opt. Express* **28**, 19457, DOI: [10.1364/oe.395367](https://doi.org/10.1364/oe.395367) (2020).

55. Gür, U. M., Arslanagić, S., Mattes, M. & Gregersen, N. Open-geometry modal method based on transverse electric and transverse magnetic mode expansion for orthogonal curvilinear coordinates. *Phys. Rev. E* **103**, 033301, DOI: [10.1103/PhysRevE.103.033301](https://doi.org/10.1103/PhysRevE.103.033301) (2021).
56. Lavrinenko, A. V., Lgsgaard, J. & Gregersen, N. *Numerical Methods in Photonics* (CRC PR INC, 2014).
57. Li, L. Formulation and comparison of two recursive matrix algorithms for modeling layered diffraction gratings. *J. Opt. Soc. Amer. A* **13**, 1024, DOI: [10.1364/josaa.13.001024](https://doi.org/10.1364/josaa.13.001024) (1996).
58. Balanis, C. A. *Antenna Theory: Analysis and Design* (Wiley John + Sons, 2016).
59. Abbarchi, M. *et al.* Poissonian statistics of excitonic complexes in quantum dots. *J. Appl. Phys.* **106**, 053504, DOI: [10.1063/1.3197848](https://doi.org/10.1063/1.3197848) (2009).
60. Baier, M. H., Malko, A., Pelucchi, E., Oberli, D. Y. & Kapon, E. Quantum-dot exciton dynamics probed by photon-correlation spectroscopy. *Phys. Rev. B* **73**, 205321, DOI: [10.1103/PhysRevB.73.205321](https://doi.org/10.1103/PhysRevB.73.205321) (2006).
61. Léger, Y., Besombes, L., Maingault, L. & Mariette, H. Valence-band mixing in neutral, charged, and Mn-doped self-assembled quantum dots. *Phys. Rev. B* **76**, 045331, DOI: [10.1103/PhysRevB.76.045331](https://doi.org/10.1103/PhysRevB.76.045331) (2007).
62. Tonin, C. *et al.* Polarization properties of excitonic qubits in single self-assembled quantum dots. *Phys. Rev. B* **85**, 155303, DOI: [10.1103/PhysRevB.85.155303](https://doi.org/10.1103/PhysRevB.85.155303) (2012).
63. <https://www.lumerical.com/products/>.
64. Mrowiński, P. & Şek, G. Modelling the enhancement of spectrally broadband extraction efficiency of emission from single InAs/InP quantum dots at telecommunication wavelengths. *Phys. B* **562**, 141–147, DOI: [10.1016/j.physb.2019.03.015](https://doi.org/10.1016/j.physb.2019.03.015) (2019).
65. Dusanowski, Ł. *et al.* Strongly temperature-dependent recombination kinetics of a negatively charged exciton in asymmetric quantum dots at 1.55 μm . *Appl. Phys. Lett.* **113**, 043103, DOI: [10.1063/1.5030895](https://doi.org/10.1063/1.5030895) (2018). [1807.02836](https://doi.org/10.1063/1.5030895).
66. Syperek, M. *et al.* Carrier relaxation dynamics in InAs/GaInAsP/InP(001) quantum dashes emitting near 1.55 μm . *Appl. Phys. Lett.* **103**, 083104, DOI: [10.1063/1.4818759](https://doi.org/10.1063/1.4818759) (2013).
67. Musiał, A. *et al.* High-Purity Triggered Single-Photon Emission from Symmetric Single InAs/InP Quantum Dots around the Telecom C-Band Window. *Adv. Quantum Technol.* **3**, 1900082, DOI: [10.1002/qute.201900082](https://doi.org/10.1002/qute.201900082) (2019).
68. Lambkin, J. D., Dunstan, D. J., Homewood, K. P., Howard, L. K. & Emeny, M. T. Thermal quenching of the photoluminescence of InGaAs/GaAs and InGaAs/AlGaAs strained-layer quantum wells. *Appl. Phys. Lett.* **57**, 1986–1988, DOI: [10.1063/1.103987](https://doi.org/10.1063/1.103987) (1990).
69. Gammon, D., Snow, E. S., Shanabrook, B. V., Katzer, D. S. & Park, D. Homogeneous linewidths in the optical spectrum of a single gallium arsenide quantum dot. *Science* **273**, 87–90, DOI: [10.1126/science.273.5271.87](https://doi.org/10.1126/science.273.5271.87) (1996). <https://science.sciencemag.org/content/273/5271/87.full.pdf>.
70. Moody, G. *et al.* Exciton-exciton and exciton-phonon interactions in an interfacial GaAs quantum dot ensemble. *Phys. Rev. B* **83**, 115324, DOI: [10.1103/PhysRevB.83.115324](https://doi.org/10.1103/PhysRevB.83.115324) (2011).
71. Ortner, G. *et al.* Temperature dependence of the zero-phonon linewidth in InAs/GaAs quantum dots. *Phys. Rev. B* **70**, 201301, DOI: [10.1103/PhysRevB.70.201301](https://doi.org/10.1103/PhysRevB.70.201301) (2004).

Acknowledgements

We acknowledge financial support from the Danish National Research Foundation via the Research Centers of Excellence NanoPhoton (DNRF147) and the Center for Macroscopic Quantum States bigQ (DNRF142). P. H. was funded by the Polish National Science Center within the Etiuda 8 scholarship (Grant No. 2020/36/T/ST5/00511) and by the European Union under the European Social Fund. N. G. acknowledges support from the European Research Council (ERC-CoG “UNITY”, Grant No. 865230), and from the Independent Research Fund Denmark (Grant No. DFF-9041-00046B).

Author contributions statement

P. H., A. S., B. W., K. Y., and E. S. designed and fabricated the device. P. H., A. M., A. H., and M. S. performed the experiments and analysed the data. U. M. G., P. M., and N. G. performed the theoretical analysis of the light propagation. P. H., A. H., M. S., and E. S. wrote the manuscript with contributions from all authors. E. S. initiated the research and with M. S. managed the project and supervised all efforts.

Additional information

The authors declare no competing financial interests. Supplementary information accompanies this paper.

Supplemental Material: Bright Quantum Dot Single-Photon Emitters at Telecom Bands Heterogeneously Integrated on Si

S-I Identification of excitonic complexes

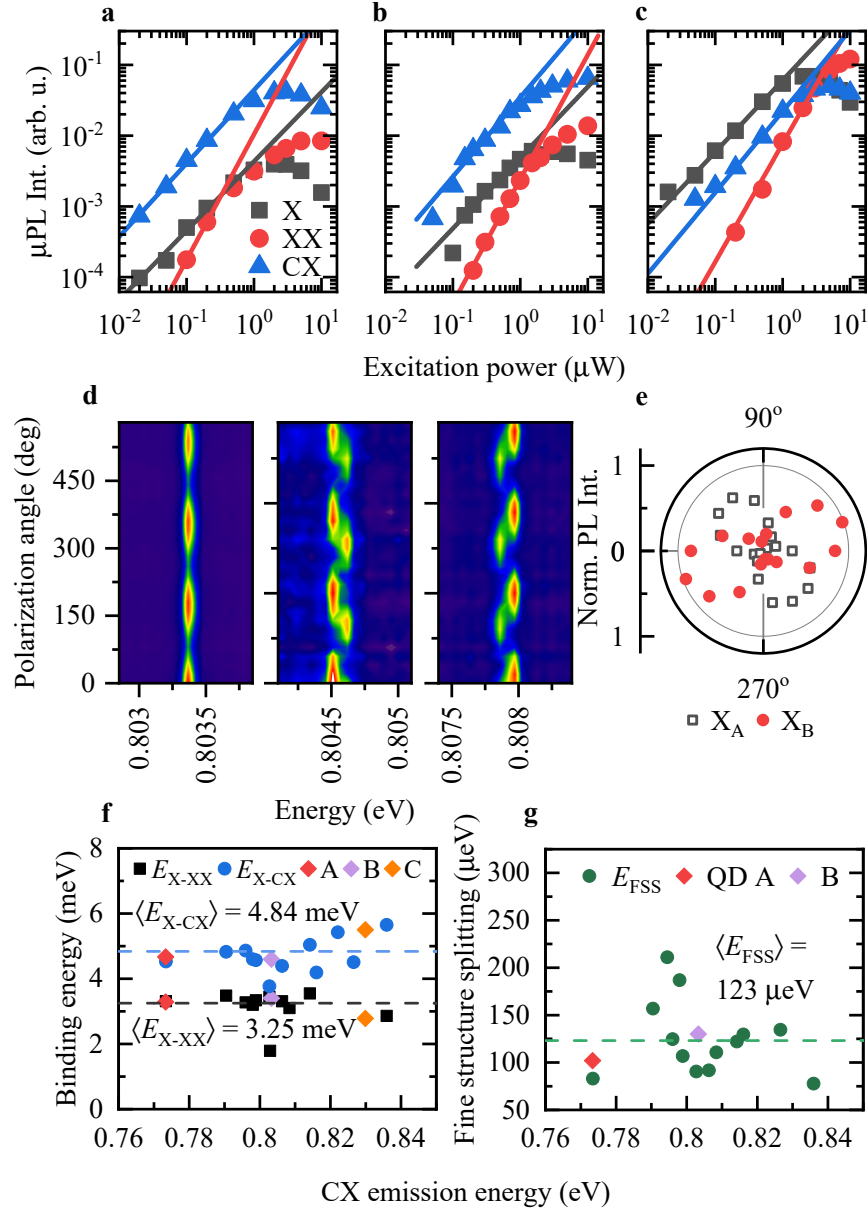


Figure S1. Excitonic complexes in InAs/InP QDs. **a-c**, Excitation power-dependent μPL intensity of identified lines in QDs: **a** A, **b** B, **c** C. **d**, Polarization-resolved μPL signal for excitonic complexes in QD B. **e**, Normalized polarization-resolved μPL intensity for X and XX in QD B. **f**, Binding energies for triions (E_{X-CX}) and for biexcitons (E_{X-XX}), with values for QDs A, B, and C marked with diamonds. **g**, Exciton fine structure splitting (E_{FSS}).

To demonstrate the optical properties of the QDs, three exemplary emitters representing the L- (QD A), C- (QD B), and S- (QD C) telecom bands are chosen, with their μPL spectra presented in Figs. 2b-2d. The excitonic complexes are identified based on the excitation power-dependent μPL intensity $I_{\mu\text{PL}}$ [shown in Supplementary Figs. S1a-S1c], and polarization-resolved μPL investigations [results shown in Supplementary Figs. S1d-S1e]. We obtain the expected^{59,60} linear, superlinear and almost quadratic power dependences for excitons, triions, and biexcitons, respectively, with the following exponents b from fitting the power dependence $I_{\mu\text{PL}} = aP^b$ to the line intensities: $b_X = 0.98 \pm 0.08$, $b_{XX} = 1.77 \pm 0.11$, $b_{CX} = 1.04 \pm 0.04$ (QD A),

$b_X = 1.00 \pm 0.15$, $b_{XX} = 1.75 \pm 0.15$, $b_{CX} = 1.12 \pm 0.18$ (QD B), and $b_X = 1.02 \pm 0.02$, $b_{XX} = 1.67 \pm 0.10$, $b_{CX} = 1.15 \pm 0.05$ (QD C), where b_X , b_{XX} , b_{CX} are exponents for the X, XX, and CX lines, respectively.

An exemplary polarization-resolved μ PL map is shown in Supplementary Figure S1d with the traces that help to unambiguously ascribe the lines, with X and XX oscillating in anti-phase (right and center panel, respectively), revealing the exciton fine structure splitting with the energy $E_{\text{FSS}} = 91 \mu\text{eV}$. The slight non-orthogonality of X states, visible in the intensities of both bright exciton (X_A and X_B) and biexciton (XX_A and XX_B) states [Supplementary Figure S1e], evidences the valence-band mixing between heavy- and light-hole states due to in-plane QD shape asymmetry and anisotropic strain effects^{61,62}. Based on the polarization dependence of the X and CX lines, we determine the degree of linear polarization $\text{DOLP} = (39.6 \pm 3.2) \%$ and the amplitude of the hole states mixing $\beta = (33.7 \pm 2.7) \%$ ⁶². For the CX, we observe the lack of the emission energy dependence on the linear polarization angle [Supplementary Figure S1d, left panel].

We perform in a similar manner the identification of complexes for other QDs in the investigated structures. Based on polarization-resolved and excitation power-dependent μ PL spectra of InAs/InP QDs in the structure with mirror which emit in the range of $1.48 \mu\text{m}$ to $1.6 \mu\text{m}$, we determine the binding energies for trions (E_{X-CX}) and for biexcitons (E_{X-XX}). The summary of determined binding energies for biexcitons and trions, and the E_{FSS} values are shown in Supplementary Figs. S1f-S1g. We find that the distributions of biexciton and trion binding energies are narrow and the values for QDs A-C are close to their typical values (see the diamonds marking values for QDs A, B, and C). We calculate the average values of $\langle E_{X-CX} \rangle = 4.84 \text{ meV}$ and $\langle E_{X-XX} \rangle = 3.25 \text{ meV}$. The obtained values are spectrally-independent and only slightly spread around the average values, therefore they help in the identification of excitonic complexes in the investigated QDs A-C. For the fine structure splitting energy, we calculate the average value of $\langle E_{\text{FSS}} \rangle = 123 \mu\text{eV}$.

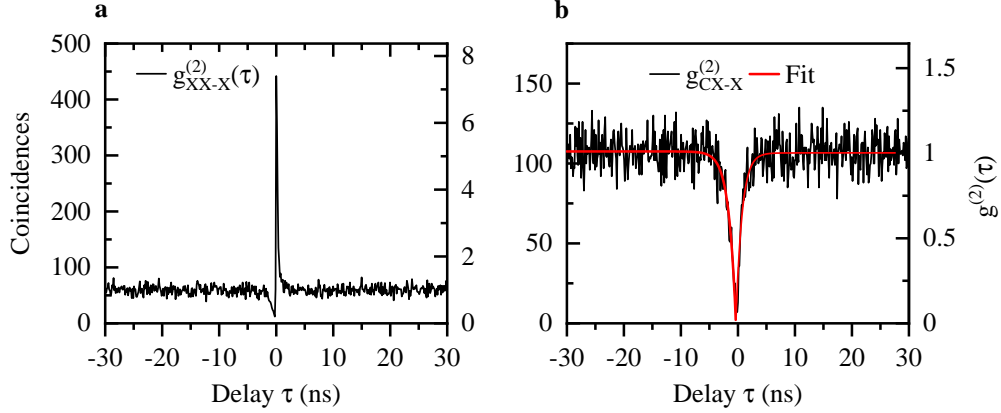


Figure S2. **a**, Cross-correlation of XX and X lines of QD C. **b**, Cross-correlation of CX and X lines of QD C with fit line (red).

Finally, for QD C we present the cross-correlation between XX-X and CX-X lines to unambiguously prove the identification of excitonic lines and the fact that they origin from the same QD. Here, X emission events are registered by the stopping detector. The histograms are shown in Supplementary Figure S1g for XX-X and Supplementary Figure S1h for CX-X cross-correlation measurements. In the case of XX-X, we find a strong bunching for positive delays, evidencing the cascaded XX-X emission, while for the CX-X case we see an asymmetric dip which we fit with the function of the form $g_{\text{CX-X}}^{(2)}(\tau) = A[1 - \exp(\tau/t_r)]$ separately for $\tau < 0$ and $\tau > 0$, where A is a scaling factor, τ is the time delay, and t_r is the antibunching time constant. We find that the t_r is different for positive and negative delays: $t_r = 1.25 \pm 0.08 \text{ ns}$ and $t_r = 1.06 \pm 0.08 \text{ ns}$, respectively, corresponding with the CX and X emission.

S-II FDTD calculations

In this section we investigate the influence of the QD position displacement in the mesa structure on the extraction efficiency. For that purpose, we employ finite-difference time-domain (FDTD) 3D Electromagnetic Simulator provided by Lumerical Inc.⁶³, as a complementary tool to the previous one based on the modal method (MM)⁵⁵. More details of the employed FDTD method can be found elsewhere⁶⁴. In order to establish convergence between the two numerical methods we first compare the results for the identical photonic mesa structures with $D = 2 \mu\text{m}$ containing a point dipole at the central position $\Delta x = 0 \text{ nm}$. Then, the FDTD approach was tuned to minimize deviation with respect to the modal method by slight change of the numerical aperture of the collected emission or the position of the 2D field-power monitor located above the mesa structure. Such tuning

mechanism is visualized in Supplementary Figure S3a as the black shaded area which overall is qualitatively similar to the results obtained by the modal method.

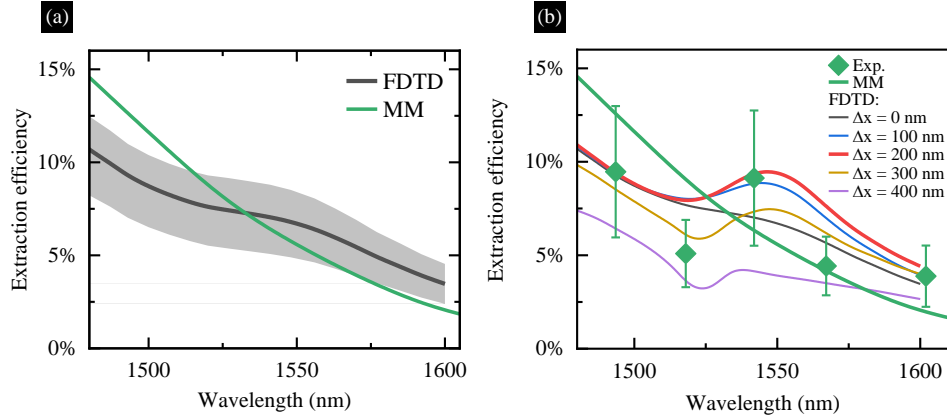


Figure S3. Analysis of the influence of the QD position in the mesa on the extraction efficiency. **a**, Comparison of calculated extraction efficiency between the FDTD and MM methods for the QD in the center of the mesa ($\Delta x = 0$ nm). The shaded uncertainty range results from different vertical screen positions ($0.8\mu\text{m}$ to $2.4\mu\text{m}$ above the mesa surface) **b**, Dispersion of the extraction efficiency for different QD displacement from the center of the mesa (Δx).

Next, such consistent FDTD model was used to calculate the dispersion of extraction efficiency for a variety of the dipole displacements in the range of $\Delta x = 0$ nm to 400 nm. Starting from $\Delta x = 100$ nm, a local enhancement of extraction efficiency around $1.55\mu\text{m}$ is already observable and this effect is further strengthened for $\Delta x = 200$ nm displacement, as it is shown in Supplementary Figure S3b. Further shift of the dipole position causes decrease of the extraction efficiency values, and taking into account the experimental results we observe the best match for QD B at $\Delta x = 200$ nm, suggesting that the QDs are placed in between $\Delta x \approx 0$ nm to 200 nm.

S-III Time-resolved microphotoluminescence for CX lines in QDs A-C

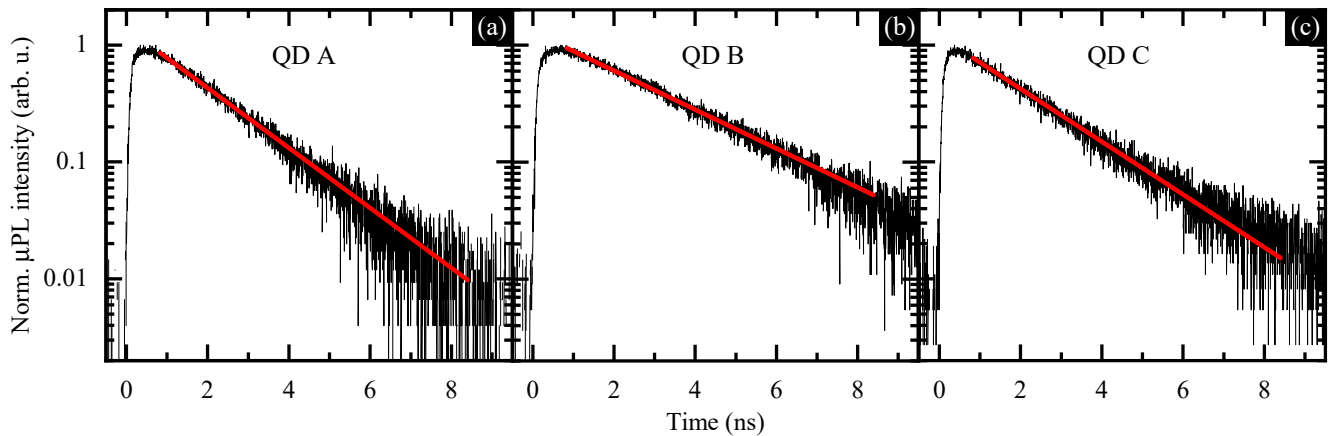


Figure S4. Time-resolved μPL traces for trions in QDs A-C: **a**, QD A, **b**, QD B, **c**, QD C. Red solid lines are fit lines to the experimental data (black lines), according to Eq. (S1).

Low-temperature ($T = 4.2$ K) time-resolved μPL (TRPL) traces registered for QDs A, B, and C are presented in Supplementary Figure S4 with solid black lines. Each trace is best fitted with a single-exponential decay function (red solid lines) to extract decay time constant τ_{PL} . We use the function of the form:

$$I(t) = A \exp(-t/\tau_{\text{PL}}), \quad (\text{S1})$$

where $I(t)$ is the TRPL intensity at time t , and A is the amplitude of the signal. The extracted τ_{PL} values are 1.69 ± 0.01 ns (QD A), 2.61 ± 0.01 ns (QD B), and 1.92 ± 0.01 ns (QD C). The τ_{PL} times are rather typical for single InAs/InP QDs, independently of their exact size and symmetry^{28,65–67} and agree with the τ_{dec} values (see comparison in Supplementary Table S2).

S-IV CW histograms

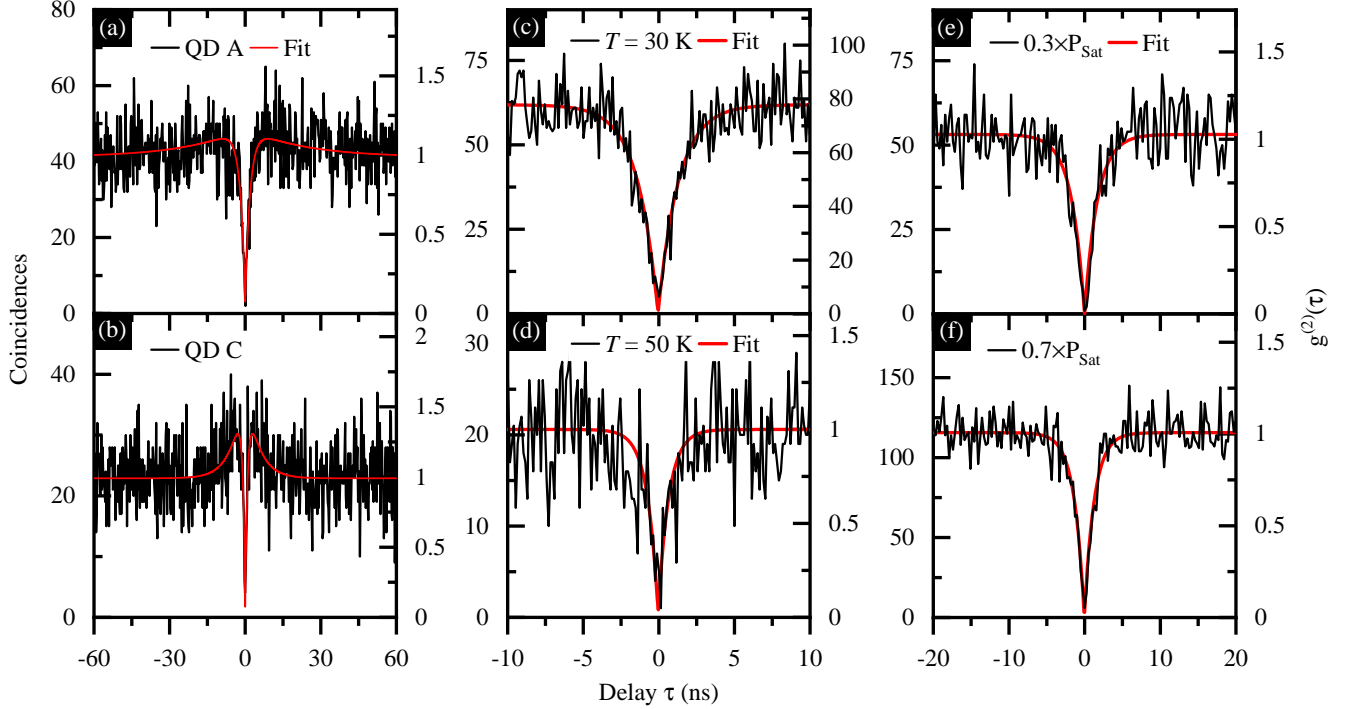


Figure S5. Evaluation of the single-photon emission purity for CX lines under cw excitation in QD **a**, A and **b**, C, and for CX line in QD B at elevated temperatures: recorded and C QD B, at **c**, $T = 30$ K, **d**, $T = 50$ K, and for **e**, $0.3 \times P_{\text{Sat}}$ and **f**, $0.7 \times P_{\text{Sat}}$.

In this section we present the histograms that broaden the discussion of the single-photon emission quality for investigated SPEs, presented in Fig. 4 in the main article. Here, we focus on the cw excitation of the CX lines, and we show the autocorrelation histograms for QDs A and C in Supplementary Figure S5a and Supplementary Figure S5b, respectively, together with fit lines. The histograms were recorded for the laser excitation power corresponding to the $0.7 \times P_{\text{Sat}}$ of the respective lines. We observe an additional weak bunching effect which we attribute to the blinking caused by the interaction with carrier traps in the QD vicinity or background doping^{47,49}, and we fit the normalized histograms with the function³¹

$$g^{(2)}(\tau) = 1 - A \exp(-|\tau|/\tau_1) + B \exp(-|\tau|/\tau_2), \quad (\text{S2})$$

where A and B are fit parameters, while τ_1 and τ_2 are antibunching and bunching time constants, respectively. The $g^{(2)}(0)$ value is obtained as $g^{(2)}(0) = 1 - A + B$. Determined parameters are $g^{(2)}(0) = 0.074$ ($\sigma = 0.062$), $\tau_1 = 1.93 \pm 0.15$ ns, and $\tau_2 = 22.7 \pm 3.0$ ns for QD A, and $g^{(2)}(0) = 0.07$ ($\sigma = 0.11$), $\tau_1 = 0.97 \pm 0.09$ ns, and $\tau_2 = 4.81 \pm 0.45$ ns for QD C. These $g^{(2)}(0)$ values are displayed in Supplementary Table S3 for their easier comparison.

Then, we show the histograms for CX in QD B registered under the same excitation conditions as in Figs. 4b-4c, except for the temperature of the structure (Supplementary Figs. S5c-S5d) and excitation power (Supplementary Figs. S5e-S5f). We fit the normalized histograms with the standard function (see Methods). For the Stirling-compatible temperatures of $T = 30$ K and $T = 50$ K we obtain almost perfect single-photon emission with the purity of $g^{(2)}(0)_{30\text{K}} = 0$ ($\sigma = 0.054$, Supplementary Figure S5c) and $g^{(2)}(0)_{50\text{K}} = 0.017$ ($\sigma = 0.096$, Supplementary Figure S5d).

Next, for the C-band QD B we study the quantum nature of the emission in the excitation power-dependent photon autocorrelation measurements under cw non-resonant excitation. Supplementary Figs. S5e-S5f present the autocorrelation histograms corresponding to the excitation of the CX line under $0.3 \times P_{\text{Sat}}$ [Supplementary Figure S5e], and $0.7 \times P_{\text{Sat}}$ [Supplementary Figure S5f], where P_{Sat} is the laser excitation power corresponding to the saturation of the line's μPL intensity. We fit the histograms (see Methods), and achieve the values of $g^{(2)}(0) = 0$ for all probed excitation powers, with $\sigma = 0.075$,

0.056, 0.038 for $0.3 \times P_{\text{Sat}}$, $0.7 \times P_{\text{Sat}}$, and P_{Sat} ¹, respectively. The increasing pump rate W_p results in the decrease of t_r so that $t_r = (1.70 \pm 0.19)$ ns, $t_r = (1.31 \pm 0.11)$ ns, and $t_r = (1.12 \pm 0.06)$ ns for $0.3 \times P_{\text{Sat}}$, $0.7 \times P_{\text{Sat}}$, and P_{Sat} , respectively.

The obtained $g^{(2)}(0)$ for CX in the QD B are repeated in Supplementary Table S4.

S-V Temperature-dependent photoluminescence of QD B

The temperature-dependent μPL of the QD B is recorded in the temperature range of $T = 5$ K to 120 K and analyzed before recording the autocorrelation histograms at elevated temperatures, shown in Fig. 4c. The spectra, the temperature-dependent quench of CX and X lines, and the linewidth broadening of the CX line are presented in Supplementary Figure S6.

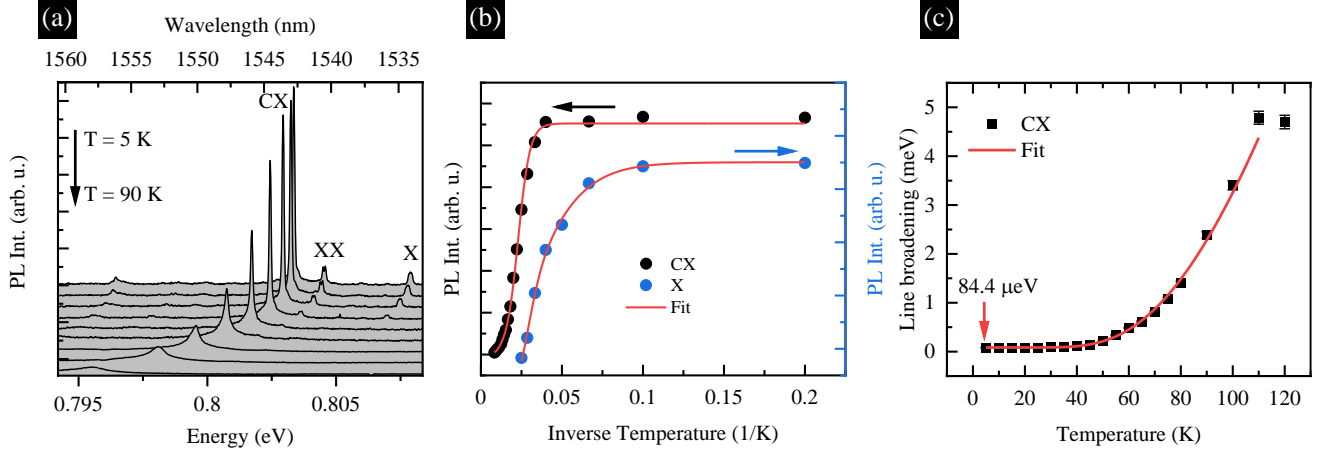


Figure S6. Analysis of the temperature-dependent μPL spectra for QD B. **a**, μPL spectra taken at different temperatures in the range of $T = 5$ K to 90 K. **b**, μPL intensity for X and CX lines fitted with the Arrhenius formula (red lines), according to Eq. (S3). **c**, Broadening of the CX line with the fitted temperature dependence of Eq. (S4).

To identify the most efficient carrier excitation channels, the temperature-dependent μPL intensity is fitted with a standard formula assuming two activation processes⁶⁸:

$$I(T) = \frac{I_0}{1 + B_1 \exp(-E_{a,1}/k_B T) + B_2 \exp(-E_{a,2}/k_B T)}, \quad (\text{S3})$$

where I_0 is the PL intensity for $T \rightarrow 0$, $E_{a,1}$ and $E_{a,2}$ are activation energies, and B_1 and B_2 are relative rates corresponding to the efficiency of involved processes. We achieve the activation energies of $E_{a,1} = 23.6 \pm 0.8$ meV and $E_{a,2} = 81.1 \pm 15$ meV for CX and $E_{a,1} = 5.0 \pm 1.5$ meV and $E_{a,2} = 22.2 \pm 7.3$ meV for X. We find that for both lines the dominant process responsible for the μPL intensity quench is the one corresponding to the $E_{a,2}$ energy, as the rates ratio $B_1 : B_2$ is 1 : 264 and 1 : 402 for CX and X lines, respectively. Interestingly, both complexes share the activation energy in the range of ~ 22 meV to 24 meV, in agreement with the value obtained for the CX line in similar QDs³⁶, where the values of $E_{a,1} = 0.8 \pm 0.5$ meV and $E_{a,2} = 23 \pm 5$ meV were reported for a CX. There, the process corresponding to the $E_{a,2}$ activation energy was attributed as the charge transfer to higher orbital states, based on the band structure calculations within the 8-band $k \cdot p$ framework. Furthermore, for a QD emitting around the $1.55 \mu\text{m}$ spectral range, the calculated energy distance for holes between their QD and WL ground states is in the range of 70 meV to 90 meV³⁶, therefore we attribute the $E_{a,2} = 81.1 \pm 15$ meV estimated for the CX as the excitation of the hole from the QD B to the WL ground state.

The temperature dependence of linewidth was fitted with the formula that includes the contribution of thermally-activated phonon sidebands to the zero-phonon line^{69,70},

$$\Gamma(T) = \Gamma(4.2\text{K}) + a \left[\exp\left(\frac{E_{\text{ph},\Gamma}}{k_B T}\right) - 1 \right]^{-1}, \quad (\text{S4})$$

where k_B is the Boltzmann constant, parameter $a = 72.8 \pm 6.8$ meV and $E_{\text{ph},\Gamma} = 27.39 \pm 0.55$ meV is an average energy of phonons. From the fitting we obtain the initial CX line broadening of $\Gamma(4.2\text{K}) = 84.4 \pm 1.2$ μeV what is above the lifetime-limited linewidth (0.5 μeV to 0.8 μeV , according to TRPL data in Supplementary Figure S4) as well as above the

¹The histogram recorded for P_{Sat} is shown in Fig. 4b

spectral resolution of the μPL setup ($\sim 25\mu\text{eV}$) and so points to the presence of spectral diffusion due to the deep charge traps in the QD vicinity, also on the etched mesa walls⁷¹. On the other hand, the initial broadening is much lower than in the previously fabricated structure with InAs/InP QDs in mesas of $340\mu\text{eV}$ ³⁶.

S-VI Summary of fitted and derived parameters

In Supplementary Table S1 we provide the fit parameters for the histograms obtained under cw laser excitation for QDs A, B, and C. The purity \mathcal{P} is defined as $\mathcal{P} = 1 - g^{(2)}(0)$. For the purity determination we take the fitted values of $g^{(2)}(0)_{\text{fit}}$ unless $g^{(2)}(0)_{\text{fit}} = 0$. In such cases, we employ the more conservative estimation of purity, utilizing the $g^{(2)}(0)_{\text{raw}} = C(0)/N$ value (see Methods for the fitting formula).

Different QDs, cw excitation			
QD	$g^{(2)}(0)_{\text{fit}}$	$g^{(2)}(0)_{\text{raw}}$	\mathcal{P}
A	0 ($\sigma = 0.11$)	0.0480	$(95.2^{+4.8}_{-6.2})\%$
B	0 ($\sigma = 0.056$)*	0.0519	$(94.8^{+5.2}_{-0.4})\%$
C	0.07 ($\sigma = 0.11$)	0.173	$(93^{+7}_{-11})\%$

* At $0.7 \times P_{\text{Sat}}$.

Table S1. Fit parameters of single-photon emission under cw excitation (Supplementary Figs. S5a-S5b for QDs A and C, Supplementary Figure S5f for QD B).

In Supplementary Table S2 we give the fit parameters for histograms obtained for the pulsed laser excitation (see Methods for the fitting formula). B is the level of background coincidences, A is a scaling parameter related to secondary photon emission, H is an average non-zero peak height, τ_{dec} and τ_{cap} are the decay and capture time constants, respectively. The corresponding histograms are shown in Fig. 4 and Supplementary Figs. S5a-S5b. We give also the μPL decay time τ_{PL} recorded in time-resolved μPL experiment (the corresponding μPL decay traces are presented in Supplementary Figure S4). The uncertainties given in Supplementary Table S2 are standard errors of the fitting procedure (σ).

QD	Different QDs, pulsed excitation					TRPL
	B	A	H	τ_{cap}	τ_{dec}	τ_{PL}
A	0.86 ± 0.05	12.49 ± 0.90	37.30 ± 0.16	0.34 ± 0.07 ns	1.91 ± 0.02 ns	1.69 ± 0.01 ns
B	13.32 ± 0.16	176 ± 15	152.35 ± 0.47	2.28 ± 0.05 ns	2.80 ± 0.02 ns	2.61 ± 0.01 ns
C	1.41 ± 0.15	11.2 ± 2.0	76.82 ± 0.58	0.44 ± 0.17 ns	1.99 ± 0.02 ns	1.92 ± 0.01 ns

* At $0.7 \times P_{\text{Sat}}$.

Table S2. Fit parameters of single-photon emission under and pulsed excitation for QDs A-C (Fig. 4a) with PL decay times (Fig. S4).

Supplementary Table S3 gives the derived $g^{(2)}(0)$ function values for pulsed excitation together with corresponding purity. We give both the $g^{(2)}(0)$ value based on the level of coincidences at $\tau = 0$ compared with H , and based on the area under the zero histogram peak. See Methods for the applied formulas with and without the background correction. The uncertainties given in Supplementary Table S3 are combined standard uncertainties based on A and H standard fitting errors.

Different QDs, pulsed excitation						
QD	Function value approach		Peak area approach			
	Fit value at $\tau = 0$		Histogram background included		Histogram background subtracted	
	$g^{(2)}(0) = B/H$	$\mathcal{P} = 1 - g^{(2)}(0)$	$g^{(2)}(0)_{\text{area}}$	$\mathcal{P}_{\text{area}}$	$g^{(2)}(0)_{\text{area}}$	$\mathcal{P}_{\text{area}}$
A	0.023 ± 0.010	$97.7 \pm 1.0 \%$	0.371 ± 0.020	$62.9 \pm 2.0 \%$	0.276 ± 0.002	$72.4 \pm 2.0 \%$
B	0.087 ± 0.017	$91.3 \pm 1.7 \%$	0.433 ± 0.018	$56.7 \pm 1.8 \%$	0.209 ± 0.018	$79.1 \pm 1.8 \%$
C	0.018 ± 0.012	$98.2 \pm 1.2 \%$	0.205 ± 0.02	$79.5 \pm 2.0 \%$	0.114 ± 0.02	$88.6 \pm 2.0 \%$

* At $0.7 \times P_{\text{Sat}}$.

Table S3. $g^{(2)}(0)$ values and corresponding purity \mathcal{P} of the single-photon emission under pulsed excitation (Fig. 4a) derived based on the fit parameters given in Supplementary Table S2.

Supplementary Table S4 displays the fit parameters obtained for CX in QD B, for the excitation-power- and temperature-dependent autocorrelation histograms. Again, for the determination of \mathcal{P} we use the fitted values of $g^{(2)}(0)_{\text{fit}}$ unless $g^{(2)}(0)_{\text{fit}} = 0$. In such cases, we utilize the $g^{(2)}(0)_{\text{raw}} = C(0)/N$ value.

QD B, cw excitation							
Excitation power series				Temperature series			
Laser power	$g^{(2)}(0)_{\text{fit}}$	$g^{(2)}(0)_{\text{raw}}$	\mathcal{P}	Temperature	$g^{(2)}(0)_{\text{fit}}$	$g^{(2)}(0)_{\text{raw}}$	\mathcal{P}
$0.3 \times P_{\text{Sat}}$	0 ($\sigma = 0.075$)	0.0188	$(98.1^{+1.9}_{-5.6}) \%$	30K	0 ($\sigma = 0.054$)	0.0808	$91.9 \pm 5.4 \%$
$0.7 \times P_{\text{Sat}}$	0 ($\sigma = 0.056$)	0.0519	$(94.8^{+5.2}_{-0.4}) \%$	50K	$0.017 (\sigma = 0.096)$	0.0486	$(98.3^{+1.7}_{-7.9}) \%$
P_{Sat}	0 ($\sigma = 0.038$)	0.0272	$(97.3^{+2.7}_{-1.1}) \%$	80K	$0.25 (\sigma = 0.19)$	0.299	$75 \pm 19 \%$

Table S4. The histogram fit parameters obtained for CX in QD B, for excitation power- and temperature-dependent autocorrelation histograms [see Figs. 4b-4c and Supplementary Figs. S5c-S5f].